



Fusion of ${}^6\text{Li}$ with ${}^{152}\text{Sm}$: Role of projectile breakup versus target deformation

P.K. Rath ^a, S. Santra ^{b,*}, N.L. Singh ^a, K. Mahata ^b, R. Palit ^c,
B.K. Nayak ^b, K. Ramachandran ^b, V.V. Parkar ^{c,1}, R. Tripathi ^d,
S.K. Pandit ^b, S. Appannababu ^a, N.N. Deshmukh ^a, R.K. Choudhury ^b,
S. Kailas ^b

^a Department of Physics, The M.S. University of Baroda, Vadodara-390002, India

^b Nuclear Physics Division, Bhabha Atomic Research Centre, Mumbai-400085, India

^c Department of Nuclear and Atomic Physics, Tata Institute of Fundamental Research, Mumbai-400005, India

^d Radiochemistry Division, Bhabha Atomic Research Centre, Mumbai-400085, India

Received 3 June 2011; received in revised form 19 September 2011; accepted 11 October 2011

Available online 21 October 2011

Abstract

Complete fusion cross sections for ${}^6\text{Li} + {}^{152}\text{Sm}$ reaction have been measured at beam energies ($E_{lab} = 20\text{--}40$ MeV) near the Coulomb barrier. The sub-barrier fusion cross sections were found to be systematically larger than those for ${}^6\text{Li} + {}^{144}\text{Sm}$, as expected from the deformed shape of the ${}^{152}\text{Sm}$ nucleus. The coupled-channels (CC) calculations including both projectile and target couplings overpredict the experimental fusion cross sections at above barrier energies. Reduced fusion cross sections for the present system at above barrier energies are found to be smaller compared to those with tightly-bound projectiles forming similar compound nuclei and also to those predicted using proximity potential. These observations along with the comparison of derived barrier distributions conclude that the complete fusion cross sections at energies above the Coulomb barrier are suppressed by $28 \pm 4\%$. A large cross section measured for incomplete fusion indicates that the above suppression is due to the loss of incident flux caused by projectile breakup. Thus the effect of both target deformation and projectile breakup are found to coexist.

© 2011 Elsevier B.V. All rights reserved.

* Corresponding author.

E-mail address: ssantra@barc.gov.in (S. Santra).

¹ Present address: Departamento de Física Aplicada, Universidad de Huelva, E-21071, Huelva, Spain.

Keywords: NUCLEAR REACTIONS $^{152}\text{Sm}(^6\text{Li}, X)$, $E = 20\text{--}40$ MeV; measured E_γ , I_γ of fusion reaction products; deduced complete fusion σ , reaction mechanism features. Comparison with coupled-channel calculations

1. Introduction

The effect of breakup of weakly bound (stable or radioactive) nuclei on fusion process is a subject of current experimental and theoretical interest [1–7]. In a recent fusion measurement involving a weakly bound projectile and a spherical target, i.e., $^6\text{Li} + ^{144}\text{Sm}$ [3], we have observed that there is a suppression of complete fusion (CF) cross section compared to the coupled-channels calculations, particularly at above barrier energies. The reduction in the CF cross section was attributed to the loss of incident flux due to the projectile breakup. The target (^{144}Sm) being spherical, its static effects on fusion cross section was negligible. However, if the target is deformed it is expected to play a significant role in governing the fusion process [8–18]. To determine the effect of deformation in addition to the effect of projectile breakup on fusion requires systematic experimental data with good precision at low bombarding energies, where penetrability effects are important. Barrier distribution extracted from these fusion excitation functions can provide additional information on the structure of the target/projectile [19,20].

The effect of target deformation on fusion cross section is expected to differ depending on whether it is static or dynamically induced [21,22]. When averaged over all orientations of a deformed nucleus [10,21], the fusion cross section becomes larger compared to a spherical nucleus. However, the dynamical effects such as excitation of the vibrational states or the rotation of the deformed nucleus during the collision can sometimes lead to reduction in fusion cross section [13,21,22]. The static deformation effects could be very important and they may show up partly through absorption below the barrier [11]. There are reports [12–14] that the fusion cross sections involving a much deformed ^{154}Sm target nucleus are considerably larger than a less deformed ^{148}Sm nucleus with strongly bound projectile ^{16}O at sub-barrier energies. Similar effects are also observed for two more projectiles ^{32}S and ^{40}Ar [14,23]. While most of the studies on the effect of target deformation on fusion cross section involve strongly bound projectiles such as ^{16}O , ^{32}S etc., the studies involving loosely bound nuclei (^6Li , ^7Li , ^9Be) with deformed targets are scarce. Fusion reactions involving loosely bound projectiles would be more revealing towards the dominance of the effects of projectile breakup or target deformation, specially at sub-barrier energies. It would be interesting to see if the sub-barrier fusion enhancement due to deformation gets further magnified with the breakup coupling or it is neutralized by the suppression of fusion cross section due to loss of incident flux caused by projectile breakup. It has also been observed that although the effect of couplings of the target inelastic states (e.g., 2^+ , 3^- vibrational states of ^{208}Pb) on elastic scattering or fusion in the systems involving tightly bound projectiles ($^{12}\text{C} + ^{208}\text{Pb}$, ^{209}Bi) are significant [24,25], it is negligible for the systems involving weakly bound projectiles ($^6, ^7\text{Li} + ^{208}\text{Pb}$, ^{209}Bi) [26,27], where the effect of projectile breakup is dominated. So, it would be interesting to investigate whether similar scenario is observed for a system with a target (^{152}Sm) having rotational inelastic states.

In this paper we present excitation function measurements for complete fusion of ^6Li with ^{152}Sm (deformed) target by recoil catcher technique followed by off-line gamma-ray spectrometry around Coulomb barrier energies. Fusion cross sections are compared with our previously measured data for $^6\text{Li} + ^{144}\text{Sm}$ [3] to investigate the isotopic target dependence. The paper is organised as follows. The details of the measurements and data analysis are described in Section 2. Coupled-channels calculations have been performed to understand the effect of target

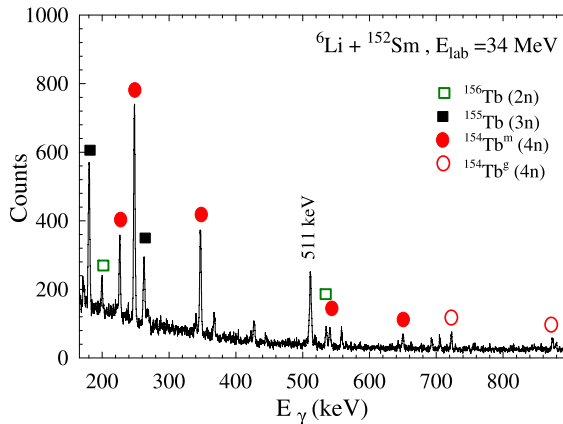


Fig. 1. (Color online.) Typical γ -ray spectrum in ${}^6\text{Li} + {}^{152}\text{Sm}$ reaction at projectile energy $E_{\text{lab}} = 34$ MeV. γ -rays from the ERs populated via CF are marked.

deformation as well as projectile couplings on fusion cross section and the details are given in Section 3.1. To see the effect of projectile breakup, the present fusion data have been compared with those involving strongly bound projectiles forming nearly same compound nucleus (${}^{12}\text{C} + {}^{141}\text{Pr}$, ${}^{20}\text{Ne} + {}^{133}\text{Cs}$) [28,29], as well as those predicted by Wong's model using the fusion barrier parameters from proximity potentials, as described in Sections 3.2 and 3.3. The continuum discretized coupled-channels (CDCC) calculations with the projectile breakup channels and their effect on fusion are discussed in Section 3.4. Discussion on incomplete fusion is given in Section 3.5. Finally, the summary and conclusions are given in Section 4.

2. Experimental details and data reduction

The experiment was performed at the 14MV BARC-TIFR pelletron facility, Mumbai using ${}^6\text{Li}$ beam incident on ${}^{152}\text{Sm}$ (98% enriched) target having thickness varying from 450–580 $\mu\text{g}/\text{cm}^2$. The targets were prepared by electrodeposition method on Al backing of thickness ~ 2 mg/cm^2 . The thickness of the targets was measured by Rutherford backscattering (RBS) using 60 MeV ${}^{16}\text{O}$ beam as well as 4 MeV proton beam. The targets with the Al backings were placed normal to the beam direction so that the recoiling nuclei, which are formed during the interaction of the projectile and the target nucleus are stopped in target + Al backing assembly. Each target was irradiated for 6–8 hours by ${}^6\text{Li}$ beam with energy $E_{\text{lab}} = 20$ –40 MeV in steps of 0.5–2.0 MeV. The beam current was ~ 40 –100 nA and the beam flux was calculated by the total charge collected in the Faraday cup placed behind the target. The reaction products stopped in the target and Al backing were identified by their characteristic gamma rays by off-line counting using HPGe detector coupled to a multichannel analyzer. The energy calibration and absolute efficiency for the HPGe detector was determined using calibrated radioactive sources viz., ${}^{152}\text{Eu}$ and ${}^{133}\text{Ba}$. The energy resolution of the HPGe detector was ~ 2.7 keV for $E_\gamma = 778$ keV and ~ 3 keV for $E_\gamma = 1408$ keV of the ${}^{152}\text{Eu}$ source. A typical γ -ray spectrum for different evaporation residues (ERs) populated via CF in ${}^6\text{Li} + {}^{152}\text{Sm}$ reaction at projectile energy $E_{\text{lab}} = 34$ MeV is shown in Fig. 1.

The excited compound nucleus formed by complete fusion decays predominantly by 2n, 3n, 4n and 5n evaporation forming the residual nuclei ${}^{156}\text{Tb}$, ${}^{155}\text{Tb}$, ${}^{154}\text{Tb}$ and ${}^{153}\text{Tb}$ either in ground

Table 1

List of identified evaporation residues in the ${}^6\text{Li} + {}^{152}\text{Sm}$ reaction along with their radioactive decay half-lives ($T_{1/2}$), γ -ray energies and intensities following their decays.

Reactions	ER	$T_{1/2}$	E_γ (keV)	I_γ (%)
${}^{152}\text{Sm}({}^6\text{Li}, 2n)$	${}^{156}\text{Tb}$	5.35 d	534.3	66.34
${}^{152}\text{Sm}({}^6\text{Li}, 3n)$	${}^{155}\text{Tb}$	5.32 d	180.1	7.45
		5.32 d	262.3	5.3
${}^{152}\text{Sm}({}^6\text{Li}, 4n)$	${}^{154}\text{Tb}^g$	21.5 h	1274.4	10.5
		21.5 h	722.1	7.7
${}^{152}\text{Sm}({}^6\text{Li}, 4n)$	${}^{154}\text{Tb}^{m1}$	9.4 h	540.2	20.0
		9.4 h	649.6	10.9
${}^{152}\text{Sm}({}^6\text{Li}, 4n)$	${}^{154}\text{Tb}^{m2}$	22.7 h	346.7	69.2
		22.7 h	1419.8	46.0
		22.7 h	225.9	26.8
${}^{152}\text{Sm}({}^6\text{Li}, 5n)$	${}^{153}\text{Tb}$	2.34 d	212	31.0
		2.34 d	170.5	6.3
${}^{152}\text{Sm}(d, 2n)$	${}^{152}\text{Eu}^{m1}$	9.274 h	841.6	14.2
		9.274 h	963.4	11.67

state (g.s.) or in metastable state (m.s.), which then decay to Gd isotopes by electron capture (EC). The respective half-lives of the decay of Tb isotopes at g.s. to Gd isotopes by EC are 5.35 d, 5.32 d, 21.5 h and 2.34 d respectively. The ${}^{154}\text{Tb}$ may also decay to ${}^{154}\text{Gd}$ from any of its two metastable states with half-lives of 9.4 h and 22.7 h. Various nuclear data values like half-lives ($T_{1/2}$), γ -ray energies (E_γ) and gamma-ray relative intensities (I_γ (%)) for ERs were taken from the table of Isotopes and Nuclear Wallet Card [30] and are given in Table 1. The gamma-ray energies given in Table 1 correspond to the transitions in the Gd isotopes resulted by the electron capture of the respective Tb isotopes. The half-lives of all the ERs of our interest are confirmed by following their activities as a function of time. Various gamma lines corresponding to the same ER having different I_γ (%) have also been used for confirmation of estimated channel cross section.

The ER cross section (σ_{ER}) at a particular beam energy E was obtained using the expression,

$$\sigma^{ER}(E) = \frac{Y\lambda}{(1 - e^{-\lambda t_{irr}})(1 - e^{-\lambda \Delta t})(e^{-\lambda t_{cool}})(N_T N_P I_\gamma \varepsilon)} \quad (1)$$

where, Y is the area under the γ -peak acquired during the interval Δt corresponding to the residual nucleus with decay constant λ ; t_{irr} is the time duration for irradiation; N_T is the number of target nuclei per unit area; N_P is the number of projectile nuclei incident on the target per unit time; t_{cool} is the time elapsed between the end of irradiation and start of counting; ε is the efficiency of the HPGe detector at the peak energy and I_γ is the intensity branching ratio associated with the particular gamma line corresponding to the residual nucleus.

Since an ER can be populated in either its ground or metastable states, the cross section of the corresponding channel is equal to the sum of the contributions from both of these states. Fig. 2 shows the ER cross sections for $4n$ channels. Total cross section for $4n$ -ER (filled circles) were obtained from the sum of the ground state of ${}^{154}\text{Tb}^g$ (hollow diamonds), 1st metastable state of ${}^{154}\text{Tb}^{m1}$ (hollow squares) and second metastable state of ${}^{154}\text{Tb}^{m2}$ (hollow triangles).

The gamma line (534.3 keV) corresponding to $2n$ channel has the contamination from $5n$ channel (533.08 keV). At low energies, the contribution from $5n$ channel is expected to be negligible because of its low cross section as well as low branching ratio, but at high energies where

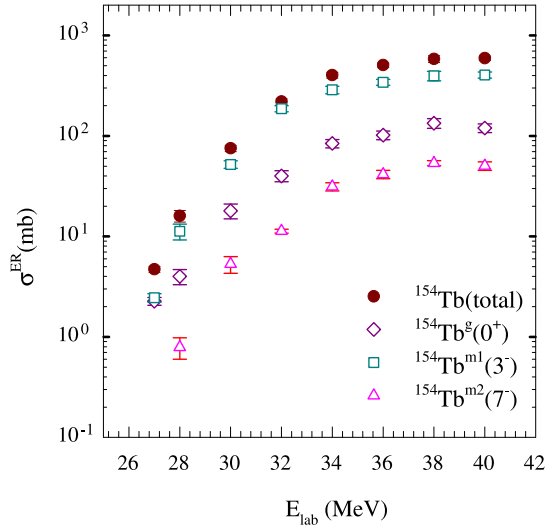


Fig. 2. (Color online.) Partial cross sections for $4n$ evaporation (filled circles) are obtained as a sum of $^{154}\text{Tb}^g$ (hollow diamonds), $^{154}\text{Tb}^{m1}$ (hollow squares) and $^{154}\text{Tb}^{m2}$ (hollow triangles).

the cross section for $5n$ channel is very high its contribution is significant and needs correction. This was done by fitting the gamma (534.3 keV) activity curve with two half lives (5.35 d for $2n$ and 2.34 d for $5n$ channels). Cross sections for $5n$ channel were obtained from independent gamma lines (212 keV and 170.5 keV) and they were used as constraints in the above fit to extract the ER cross section for the $2n$ channel only for few high energy data points.

The measured excitation functions for individual ER channels thus obtained are shown in Fig. 3. The ER data for $2n$, $3n$, $4n$ and $5n$ channels are represented by triangles, stars, diamonds and squares respectively.

To study the relative contributions of different ER channels to the CF, statistical model (SM) calculations were performed using the code PACE [31]. The optical model potentials of Perey and Perey [32] are used for neutron and proton, while that of Huizenga and Igo [33] for alpha particle emission. For sub-barrier energies the ℓ -distributions obtained from coupled-channels calculations were used as input. Two important parameters in the statistical model calculations are (i) transmission co-efficient of the outgoing particles and (ii) level density of the residual nuclei. The transmission coefficients are calculated by Hill-Wheeler formula [34]. The level density parameter is ' a ' = A/K MeV $^{-1}$, where A is the mass number of the residual nucleus and K is a free parameter. The ER cross sections for $2n$, $3n$, $4n$ and $5n$ channels predicted by SM calculations with three different level density parameters are shown in Fig. 3(a). The ratio of present experimental data of σ_{4n} to σ_{3n} is shown in Fig. 3(b). The ER cross sections obtained from both theory (σ_{ER}^{PACE}) and experiment (σ_{ER}^{expt}) in terms of percentage fraction of the complete fusion cross section (σ_{CF}^{PACE}) are shown in Fig. 3(c). Results for each ER are shown by dash-dot-dot, medium dashed and solid lines corresponding to $a = A/9$ MeV $^{-1}$, $A/10$ MeV $^{-1}$ and $A/11$ MeV $^{-1}$ respectively. It can be observed that the SM results with $K = 10$ MeV provide the best description of the ratio of present experimental data of σ_{4n} to σ_{3n} over the entire energy range.

The dominant channels for most of the energy range were found to be $3n$ and $4n$ ERs except few points at extreme low energies where the contribution from $2n$ channel is significant.

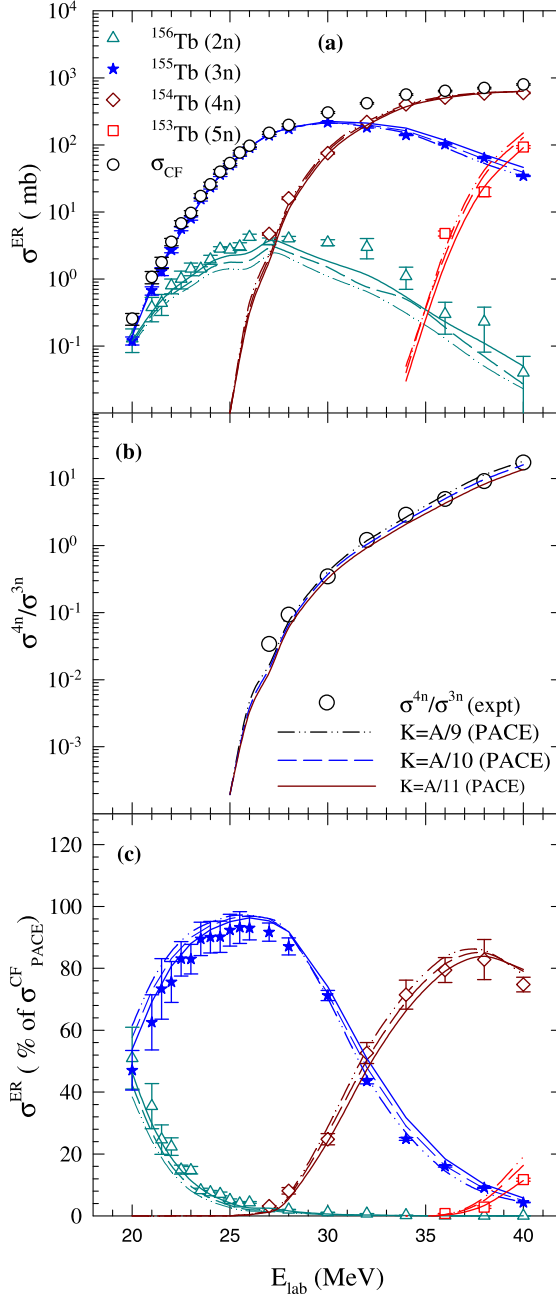


Fig. 3. (Color online.) Measured ER cross sections for ^{156}Tb — 2n-channel (triangles), ^{155}Tb — 3n-channel (stars), $^{154}\text{Tb}^{(g+m)}$ — 4n-channel (diamonds) and ^{153}Tb — 5n-channel (squares). Results of SM calculations corresponding to the level densities of $a = A/9 \text{ MeV}^{-1}$, $A/10 \text{ MeV}^{-1}$ and $A/11 \text{ MeV}^{-1}$ are shown as dash-dot-dot, medium-dashed and solid lines respectively for each of the above channels. Open circles represent the experimental fusion cross sections data. (b) Comparison of the ratio of σ_{4n} to σ_{3n} obtained from PACE using different level densities with the experimental data. (c) Normalized ER cross sections from the measurement and SM calculations (with different level densities) showing the percentage contribution to CF cross section.

Table 2

Complete fusion data are included in the 5th column of this table as a result of a combination of experimental data — 4th column — a sum of ER cross sections for $2n$, $3n$, $4n$ and $5n$ evaporation channels, and the ratio R_σ from PACE calculations included in the 3rd column.

E_{lab} (MeV)	$E_{c.m.}$ (MeV)	R_σ	$(\sigma_{2n+3n+4n+5n})^{expt}$ (mb)	σ_{CF}^{expt} (mb)
20.0	19.2	1.00	0.26 ± 0.05	0.26 ± 0.05
21.0	20.2	1.00	1.07 ± 0.22	1.07 ± 0.22
21.5	20.7	1.00	1.77 ± 0.34	1.77 ± 0.34
22.0	21.2	1.00	3.57 ± 0.45	3.57 ± 0.45
22.5	21.6	1.00	6.74 ± 0.65	6.74 ± 0.65
23.0	22.1	1.00	9.62 ± 0.80	9.64 ± 0.80
23.5	22.6	1.00	17.3 ± 1.5	17.3 ± 1.5
24.0	23.1	1.00	25.7 ± 2.1	25.8 ± 2.1
24.5	23.6	0.99	39.4 ± 3.2	39.7 ± 3.2
25.0	24.1	0.99	53.4 ± 4.3	53.7 ± 4.3
25.5	24.5	0.99	76.2 ± 6.1	76.8 ± 6.1
26.0	25.0	0.99	96.4 ± 5.7	97.0 ± 5.7
27.0	26.0	0.99	150 ± 7.0	151 ± 7.0
28.0	26.9	0.99	196 ± 9.0	198 ± 9.0
30.0	28.9	0.99	301 ± 10	304 ± 10
32.0	30.8	0.99	413 ± 12	418 ± 12
34.0	32.7	0.99	555 ± 15	563 ± 15
36.0	34.6	0.98	626 ± 16	637 ± 16
38.0	36.6	0.97	682 ± 18	705 ± 19
40.0	38.5	0.93	739 ± 18	797 ± 20

Presence of $5n$ channel was observed only at higher energies but its contribution was found to be $\leq 10\%$. From PACE calculations (with $K = 10$ MeV), it was found that the sum of the measured ER cross sections corresponding to $2n$, $3n$, $4n$ and $5n$ channels (i.e., $\sigma_{2n} + \sigma_{3n} + \sigma_{4n} + \sigma_{5n}$) accounts for about 97–100% of the complete fusion (σ_{CF}) in the entire energy range of our interest except at $E_{lab} = 40$ MeV. Thus the contribution from the missing channels (e.g., the charged particles like p and α evaporation channels) that have not been measured is found to be negligible ($\leq 3\%$). The ratio of the combined ER cross section to the fusion cross section (i.e., $R_\sigma = \sum \sigma_{xn}/\sigma_F$, for $x = 2, 3, 4$ and 5) was calculated from the PACE results as given in Table 2. The complete fusion cross sections (σ_{CF}^{expt}) are determined by dividing the cumulative experimental cross section of four channels (i.e., $\sigma_{2n}^{expt} + \sigma_{3n}^{expt} + \sigma_{4n}^{expt} + \sigma_{5n}^{expt}$) by the ratio R_σ following the procedure of Ref. [3]. The values of σ_{CF}^{expt} are given in Table 2 and also plotted in Fig. 3(a) as open circles which clearly shows the dominance of σ_{3n} and σ_{4n} over the entire energy range. Only for the lowest three energies i.e., $E_{lab} = 20, 21$ and 21.5 MeV, the fractional contribution of σ_{2n} to σ_{CF} is significant (25–50%) where the agreement between the data and the PACE prediction is good.

The errors on σ_{CF}^{expt} were estimated directly from the errors attributed to the measured ER cross sections. It can be observed that the errors are minimum ($\sim 2.5\%$) for the highest beam energies and they increase slowly as one goes down in energy to a maximum of $\sim 20\%$ at the lowest energy. The errors are mainly due to the statistical uncertainties but having small contributions from systematic uncertainties. Since the contributions of the charged particle evaporation channels to CF are small ($\leq 3\%$ for $E_{lab} = 20$ – 38 MeV), the uncertainties on the estimation of these missing cross sections are negligible. Care has been taken to limit the systematic uncertainties that could arise from different sources such as (i) current integrator reading, (ii) target thickness,

(iii) detector efficiency, (iv) estimation of gamma yield, etc. The current integrator reading has been calibrated using standard Keithley current source. The target thicknesses have been cross checked by two measurements using different ion beams (proton and ^{16}O) for elastic scattering measurements at backward angles. The absolute energy dependent detector efficiency has been measured every ten to twelve hours during off-line gamma counting using standard radioactive sources of ^{152}Eu and ^{133}Ba and found to remain invariant with time during the whole experiment. However, the uncertainty ($\sim 1\%$) in the fitting parameters of the efficiency curve has been taken into account in the final error of the ERs. So, most of the errors on ER cross sections are due to the uncertainties on gamma yield extraction and gamma statistics. For lowest three beam energies, the contribution from $2n$ ER channel to CF is substantial and the large uncertainties on σ_{2n} lead to large errors in σ_{CF}^{expt} .

To see the isotopic target dependence if any, the experimental CF cross sections obtained for the present system have been compared with those for $^6\text{Li} + ^{144}\text{Sm}$ [3]. The reduced fusion cross sections “ $\sigma_{CF}^{expt} / (A_P^{1/3} + A_T^{1/3})^2$ ” as a function of reduced energy “ $E_{c.m.} / [Z_P Z_T / (A_P^{1/3} + A_T^{1/3})]$ ” for the two systems are shown in Fig. 4(a). The above normalization was made following the prescription by Gomes et al. [35] to remove the geometrical dependence. The solid and dashed lines correspond to the CC calculations with only target inelastic couplings for $^6\text{Li} + ^{152}\text{Sm}$ and $^6\text{Li} + ^{144}\text{Sm}$ systems respectively. Details of the calculations are given in the following section and Ref. [3]. To emphasize the low energy enhancement for the present system, the ratio of the CF cross sections of the present system to those for $^6\text{Li} + ^{144}\text{Sm}$ is also plotted in Fig. 4(b). The calculated ratio represented by the dash-dot line shows similar trend as that of the data. These comparisons reveal that although the CF cross sections at above-barrier energies are of similar order, they are much enhanced for the present system at sub-barrier energies as expected from the influence of the deformed ^{152}Sm target nucleus compared to that of spherical ^{144}Sm nucleus. Similar effects have also been observed for the systems involving different isotopes of Sm but with strongly bound projectiles e.g., $^{16}\text{O} + ^{148,150,152,154}\text{Sm}$ [12,13], $^{40}\text{Ar} + ^{144,148,154}\text{Sm}$ [14] and $^{32}\text{S} + ^{144,154}\text{Sm}$ [23]. This implies that the qualitative effect of the target deformation on sub-barrier fusion, i.e., enhancement is independent of whether the projectile is weakly- or strongly-bound.

The barrier distributions derived from the above experimental fusion cross sections for two systems are also compared as shown in Fig. 4(c). There is no major difference found in the main peaks of the two barrier distributions. However, the shoulder structure at high energy region looks to be more prominent for the $^6\text{Li} + ^{152}\text{Sm}$ compared to the one for $^6\text{Li} + ^{144}\text{Sm}$. Due to the large error bars on the barrier distribution in this energy region, no conclusion can be drawn on whether this difference is due to the effect of target deformation.

3. Discussions

3.1. Coupled-channels calculations

Coupled-channels calculations were performed using the modified version of CCFULL [36] that can include the effect of projectile ground state spin and the projectile excitation. To make a sensible coupled-channels calculation it is important to choose a proper set of potential parameters. The best way to do this is to find some experimental quantity that will constrain these parameters. In the present measurement, there could be two constraints: the experimental fusion excitation function at high energies or the average experimental fusion barrier. Since the barrier distribution is more sensitive to the structure of the interacting nuclei compared to the fusion ex-

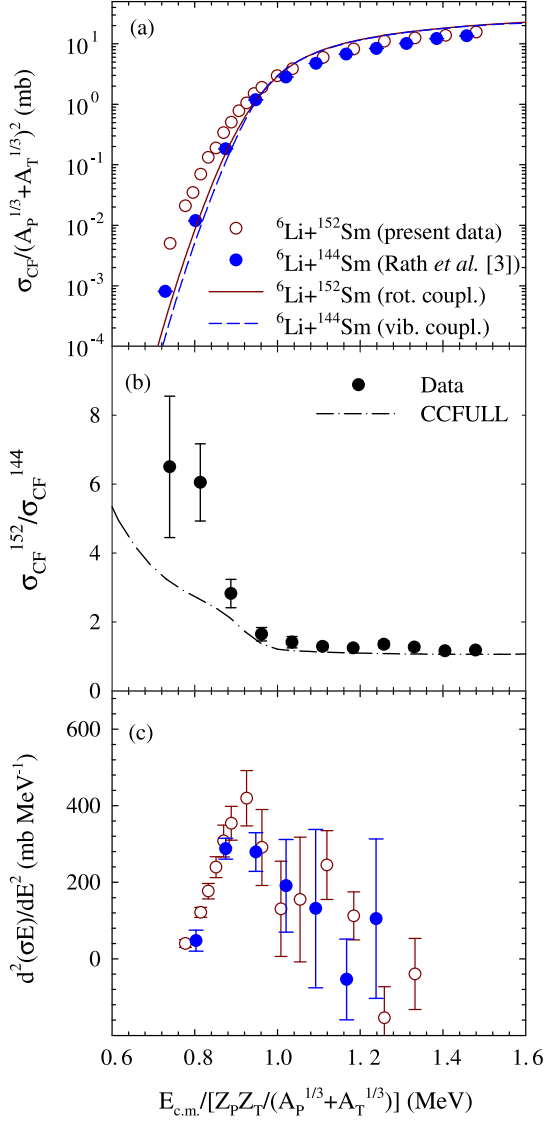


Fig. 4. (Color online.) (a) Reduced fusion cross section data and calculations versus normalized energy for present system (${}^6\text{Li} + {}^{152}\text{Sm}$) compared with those for ${}^6\text{Li} + {}^{144}\text{Sm}$ by Rath et al. [3]; (b) Ratio of the above cross sections versus normalized energy showing the target dependence; (c) Barrier distributions derived from the fusion cross sections of (a).

citation function, in the present calculations we have used the average experimental fusion barrier as the constraint. The weighted average of the experimental barrier distribution was found to be 25.1 ± 0.2 MeV. For CC calculations, the initial potential parameters chosen are obtained from the parametrization of Broglia and Winther (BW) [37] and their values in Woods–Saxon form are equal to $V_0 = 42.6$ MeV, $r_0 = 1.02$ fm, and $a_0 = 0.65$ fm. To reproduce the experimental barrier of $V_B = 25.1$ MeV and remove the oscillatory behavior of fusion cross section at high energies

the depth of the real potential was increased. The final parameters that are used in the present CC calculations are: $V_0 = 131$ MeV, $r_0 = 1.01$ fm, and $a_0 = 0.64$ fm. Once the potential parameters are fixed, one needs to find the possible channels along with their coupling parameters that are to be coupled.

CC calculations were made first with only target inelastic states. The target (^{152}Sm) being a deformed nucleus in its ground state, both quadrupole (2^+ , 0.122 MeV) and hexadecapole (4^+) rotational states with deformation parameters $\beta_2 = 0.26$ and $\beta_4 = 0.05$ [38] are coupled. The results of the CC calculations with no couplings and only target couplings are shown in Fig. 5(a) as dotted and dash-dot lines respectively. It can be seen that at energies below the barrier, there is a large enhancement in the fusion cross sections calculated with only target couplings compared to the uncoupled values. However, at above-barrier energies, it can be seen that the coupled results overpredict the measured fusion data. The barrier distribution, $d^2(\sigma E)/dE^2$, obtained from both the experimental and the calculated fusion cross sections are shown in Fig. 5(b).

To improve the shape of the calculated barrier distribution the projectile couplings were also included. In addition to the reorientation of the projectile ground state (1^+) with spectroscopic quadrupole moment, $Q = -0.082$ fm², the unbound 1st excited state (3^+ , 2.186 MeV) was also included as done in Refs. [3,39]. This however is a considerable simplification and does not reflect the realistic breakup couplings. A value of $B(E2; 1^+ \rightarrow 3^+) = 21.8$ e²fm⁴ was used for the 3^+ (2.18 MeV) unbound excited state (same as in Ref. [39]). The parameters for the projectile couplings that were used in the CCFULL calculations are: β_{00} (i.e., β_2 for the ground state reorientation) = -0.079 , β_{01} (i.e., β_2 for the transition between the ground and the first excited states) = 1.51, and β_{11} (i.e., β_2 for the reorientation of the 1st excited state) = 1.51. Inclusion of both target as well as projectile couplings (dashed line) further enhances the fusion cross sections at sub-barrier energies. However, the fusion cross sections at above-barrier energies were found to be insensitive to the projectile couplings. It should be emphasized that the measured fusion cross sections at above-barrier energies agree very well with the calculated ones when multiplied by a factor of 0.72 (solid line), implying that there is an overall suppression of $\sim 28\%$ of the fusion cross section in this energy range compared to the ones predicted by CCFULL. An uncertainty of $\pm 4\%$ in the suppression factor is estimated from the uncertainties in V_B and σ_{CF} . It was also interesting to find that the barrier distribution derived from the calculated fusion with full couplings when normalized by a factor of 0.72 (solid line) agrees quite well with the experimental distribution (filled circles).

3.2. Fusion using proximity potential

CF cross sections for the present system were compared to those predicted using the “Proximity potentials” [40,41]. These potentials are parameterized from the existing fusion data in the literature for many systems mostly with strongly bound projectiles. Fusion barrier parameters, i.e., barrier height and barrier radius, can be obtained by adding the Coulomb potential with the proximity potentials as done by Dutt et al. [42] and they can be used to predict the fusion cross section. The original version of this potential (Proximity 1977) was described by Blocki et al. [40], which was later modified and renamed as “Proximity 1988” by Reisdorf [41] to incorporate more refined mass formula of Moller and Nix [43,44]. Myers and Swiatecki [45], using their concept of droplet model, have updated the values of nuclear radii and nuclear surface tension coefficients in the latest version of the above potential and named as “Proximity 2000”. Using 1977, 1988 and 2000 forms of proximity potentials and corresponding expressions for the fusion barrier parameters, the barrier heights were calculated to be 25.0 MeV, 24.5 MeV and 24.9 MeV,

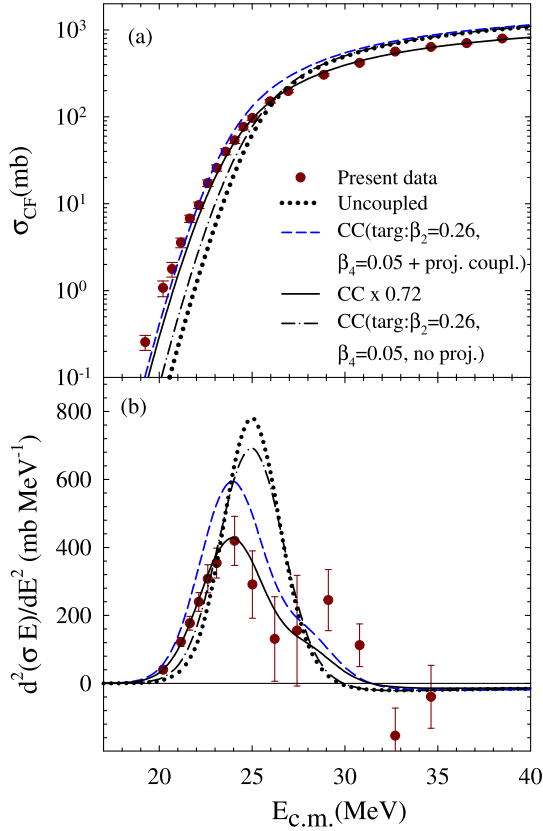


Fig. 5. (Color online.) (a) Complete fusion cross section (filled circles) and (b) corresponding barrier distribution (filled circles) for ${}^6\text{Li} + {}^{152}\text{Sm}$ compared with no couplings (dotted lines), only target couplings (dash-dot lines), projectile + target couplings (dashed lines) results from CCFULL [36] calculations. Solid lines are obtained by multiplying the CCFULL results with full couplings by a factor of 0.72.

and barrier radii as 9.91 fm, 10.18 fm and 9.98 fm respectively. Using the above parameters in simplified Wong's formula, the fusion cross sections were calculated and the results are shown as short-dashed, dotted and long dashed lines in Fig. 6 respectively. It was observed that the fusion cross sections provided by proximity potentials are required to be scaled down by factors 0.74 (dash-dot line), 0.68 (solid line) and 0.72 (dash-dot-dot line) respectively to reproduce the experimental data (filled circles) at above barrier energies. This implies that the measured fusion cross sections at higher energies are suppressed by ~ 26 – 32% compared to the calculations using proximity potentials, which are consistent with our conclusions on fusion suppression that we obtained from the CC analysis. These observations indicate that projectile breakup may be playing a crucial role in reducing the flux from the entrance channel and leading to the suppression of complete fusion cross section.

3.3. Comparison with tightly bound projectiles

In Fig. 7, the CF cross sections for the present system are compared with those for two other systems ${}^{12}\text{C} + {}^{141}\text{Pr}$ [28] and ${}^{20}\text{Ne} + {}^{133}\text{Cs}$ [29] forming nearly same compound nucleus ${}^{153}\text{Tb}$.

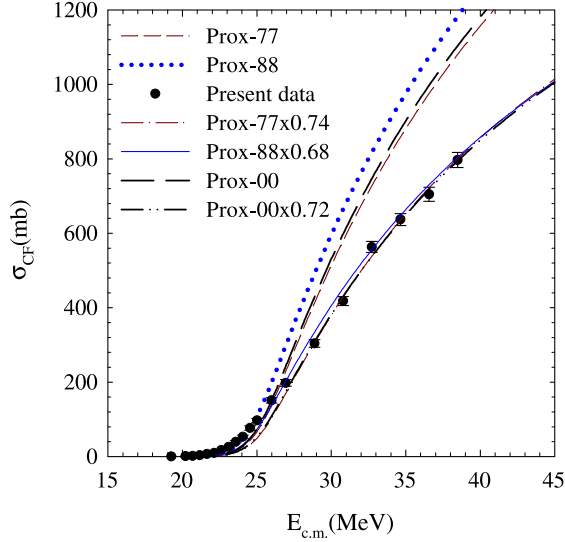


Fig. 6. (Color online.) Fusion cross sections predicted by Wong's model using proximity potentials version 1977, 1988 and 2000 are represented by short-dashed, dotted and long dashed lines respectively. Dash-dot, solid and dash-dot-dot lines are obtained by multiplying the above results by 0.74, 0.68 and 0.72 respectively. Filled circles correspond to the measured CF data for ${}^6\text{Li} + {}^{152}\text{Sm}$ reaction.

Here, the CF cross sections normalized to $(A_P^{1/3} + A_T^{1/3})^2$ are plotted as a function of normalized energy $E_{c.m.}/[Z_P Z_T / (A_P^{1/3} + A_T^{1/3})]$, similar to Fig. 4. Although the fusion cross section for the reactions involving strongly bound projectiles (${}^{12}\text{C} + {}^{141}\text{Pr}$ and ${}^{20}\text{Ne} + {}^{133}\text{Cs}$) are not very precise, it can be observed that the reduced fusion cross sections for ${}^6\text{Li} + {}^{152}\text{Sm}$ are in general smaller than those for the former. It further confirms that the fusion cross section for the present system at above-barrier energies is suppressed. It may be noted that the suppression in fusion compared to the ones for the reactions induced by tightly-bound projectiles seems to be smaller than the ones predicted by CCFULL. However, due to the low precision of literature data for ${}^{12}\text{C} + {}^{141}\text{Pr}$ and ${}^{20}\text{Ne} + {}^{133}\text{Cs}$ reactions no definite conclusions be made on the value of the suppression factor.

3.4. Breakup coupling

Since CCFULL does not have the provision to include the realistic breakup coupling in the CC calculations, one can use FRESKO [46] to understand the effect of projectile breakup on fusion. To see the effect of both projectile breakup as well as target excitations together in an approximate way as done in Ref. [27], one can first calculate the polarization potential due to breakup coupling using FRESKO and then use the effective (bare + polarization) potential as an input to the FRESKO where only target excitations are coupled. Since we already know about the effect of the target deformation from the CC calculations using CCFULL, it would be interesting to see the effect of projectile breakup employing FRESKO and find whether the results qualitatively agree with the conclusion of 'CF suppression due to projectile breakup'. However, FRESKO calculations using cluster-folded potential with long range imaginary part for the entrance channel interaction do not provide the CF cross section. Instead, the cumulative absorption cross section by the long range imaginary potential equals to the sum of the cross sections for

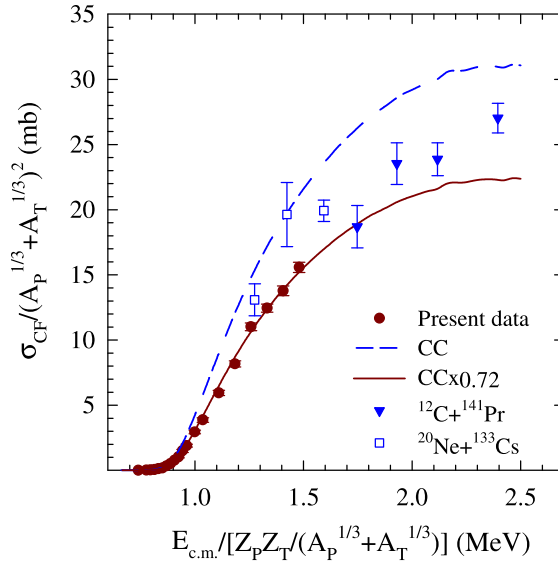


Fig. 7. (Color online.) Reduced fusion cross section as a function of reduced energy for the present system (filled circles) along with two other reactions forming the same compound nucleus i.e., $^{12}\text{C} + ^{141}\text{Pr}$ [28] (filled triangles) and $^{20}\text{Ne} + ^{133}\text{Cs}$ [29] (hollow squares). The dashed line represents the CC results and the solid line corresponds to the CC results multiplied by a factor of 0.72.

CF, ICF, transfer and target inelastic reactions. In a second method, fusion is calculated by the barrier penetration model (BPM) as done by Rusek et al. [6]. But the BPM fusion too may not explain the CF data as mentioned by Keeley et al. [2] and also observed recently by Santra et al. for $^6\text{Li} + ^{209}\text{Bi}$ [27]. Thus, one can obtain a reasonable cross section for CF only when the information on the cross sections for the remaining reaction channels are available. Despite these difficulties one can still perform the FRESKO calculations including only the projectile excitations in the continuum and find the effect of breakup on fusion to see whether it is consistent with the present experimental observations.

So, the continuum discretized coupled channels (CDCC) calculations are performed using FRESKO- version 2.8 to understand the effect of projectile breakup coupling on fusion. The projectile (^6Li) is assumed to be a cluster of α and d with a breakup threshold of 1.48 MeV. The projectile excited states in the continuum up to 7 MeV above the breakup threshold are coupled. Each discretized state is assigned with $L = 0, 1$ and 2 , where L is the relative angular momentum between the two breakup fragments (α and d). Both resonant and non-resonant states in the continuum are included. For s - and p -waves, the continuum was discretized into 14 bins of equal width in the momentum of αd relative motion. In the presence of resonances for d -waves, the discretization of the continuum was slightly modified in order to avoid double counting. Three resonant states, with widths corresponding to 0.1 MeV, 2.0 MeV and 3.0 MeV, respectively, were also treated as momentum bins, but with finer steps. Reorientation coupling is also included. The target is assumed to be in the ground state.

The cluster-folded potential obtained from the two fragment-target potentials ($V_{\alpha+^{152}\text{Sm}}$ and $V_{d+^{152}\text{Sm}}$) was used for the entrance channel interaction potential ($V_{^6\text{Li}+^{152}\text{Sm}}$). The potential parameters used for $V_{\alpha+^{152}\text{Sm}}$ ($V_{d+^{152}\text{Sm}}$) are taken from Ref. [47] ([48]), and the values are $V_0 = 60.5$ (91.82) MeV, $r_0 = 1.107$ (1.013) fm, $a_0 = 0.607$ (0.938) fm for real part and $W =$

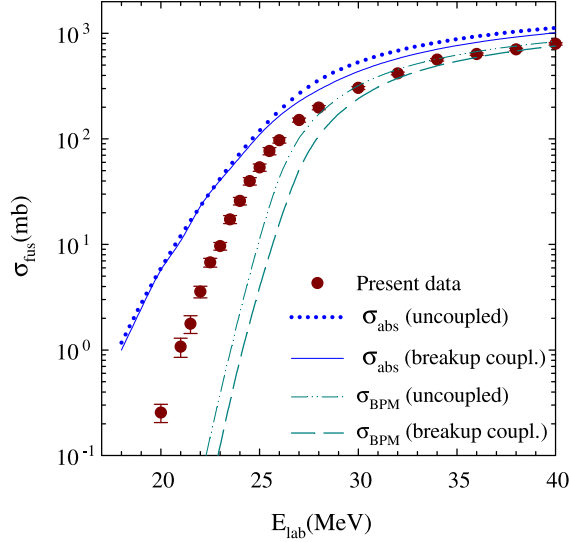


Fig. 8. (Color online.) Shown are the results of FRESKO calculations for the fusion cross sections obtained by cumulative absorption and barrier penetration with and without breakup coupling.

18.72 (21.04) MeV, $r_w = 1.035$ (1.116) fm, $a_w = 0.735$ (0.581) fm for the imaginary part. The radius parameter used for the Coulomb term is 0.964 (1.011) fm. The $\alpha + d$ binding potentials are same as those used in Ref. [49]. Two separate potentials were used for (i) ground state and s-wave continuum and (ii) p- and d-wave continuum. These potentials were chosen as they reproduce the resonances (energies and widths) correctly [50].

The dynamic polarization potential generated due to the breakup coupling in the CDCC calculations was found to be repulsive around the nuclear surface region for all the beam energies of our interest, similar to that observed in our recent study for ${}^6\text{Li} + {}^{209}\text{Bi}$ [27]. The effective (bare + polarization) potential reduces the absorption/penetration of the flux from the entrance channel into the attractive potential well. The Fusion cross sections obtained by cumulative absorption and barrier penetration model from the CDCC calculations are shown in Fig. 8. The uncoupled (coupled) results for the above two methods are represented by dotted and dash–dot–dotted (solid and long-dashed) lines respectively. It can be observed that the fusion cross sections with breakup coupling obtained by both the methods are systematically lower than the uncoupled ones at energies above the Coulomb barrier. Thus, these results qualitatively agree with our earlier conclusion on the fusion suppression due to projectile breakup.

3.5. Incomplete fusion

Incomplete fusion cross sections due to the capture of any of the breakup fragments, i.e., α or d by the target were investigated. Since the ERs formed after α -capture, e.g. ${}^{155}\text{Gd}$ (1n-ER) and ${}^{154}\text{Gd}$ (2n-ER) are all stable, it was not possible to measure their formation cross section by offline gamma-ray spectrometry.

However, for d -capture there are few ER channels with measurable half-lives. The dominant channels of d -capture are expected to be 1n and 2n ERs as per PACE predictions at deuteron energies equal to one-third of the beam (${}^6\text{Li}$) energies. Since the residue after 1n evaporation

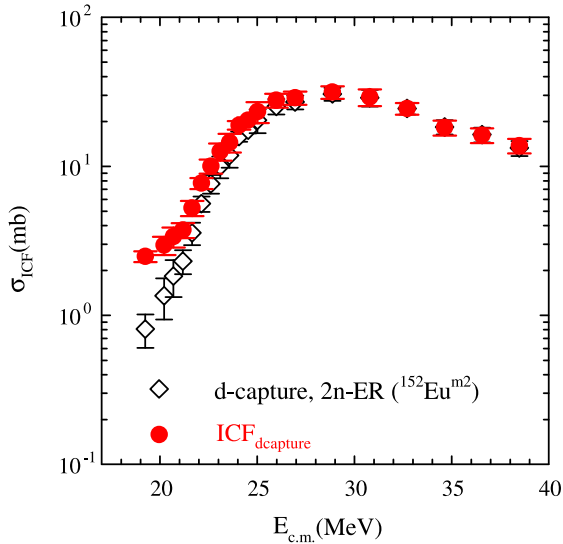


Fig. 9. (Color online.) ICF cross sections (filled circles) contributed by d -capture which are estimated from the formation cross section of $^{152}\text{Eu}^{m2}$ i.e., metastable state of $2n$ -ER channel (hollow diamonds).

following d -capture is stable, its cross section could not be measured. For $2n$ channel there could be contributions from the decay of $^{152}\text{Eu}^g$, $^{152}\text{Eu}^{m1}$ and $^{152}\text{Eu}^{m2}$ states with half-lives of 13.542 y, 9.274 h and 96 m respectively. Here m_1 and m_2 correspond to two metastable states and g corresponds to ground state of ^{152}Eu . Since the half-life of $^{152}\text{Eu}^g$ is very large, the contributions from its metastable states were only possible to measure. Out of the two metastable states, only the first metastable state with half-life of 9.274 hr has clearly been identified and the cross sections are extracted as shown as hollow diamonds in Fig. 9. The cross section for second metastable state ($t_{1/2} = 96$ m) could not be extracted accurately because of the contamination of its characteristic gamma line (89.85 KeV) with 88.97 keV gamma of ^{156}Tb corresponding to $2n$ -ER of CF.

The experimental cross section for d -capture has been estimated from experimental $2n$ -ER ($^{152}\text{Eu}^{m1}$) channel cross section by scaling with PACE predicted fusion for $d + ^{152}\text{Sm}$ reaction at energies $E = E_{lab}/3$. Results are shown as filled circles in Fig. 9. Since d -capture is only part of the ICF the above cross sections are considered to be as lower limits of the ICF.

The above ICF channel that we have discussed so far may also get populated via deuteron transfer i.e., $^{152}\text{Sm}(^6\text{Li}, \alpha)$ reaction. It is difficult to distinguish between these two contributions from our present measurement. However, one can conclude that a significant cross section of ICF observed above is probably due to breakup. Further theoretical and experimental investigations will be required to pin down this point definitively.

4. Summary and conclusions

The complete fusion cross sections for $^6\text{Li} + ^{152}\text{Sm}$ reaction have been measured at energies near and above the Coulomb barrier. The decay of the compound nucleus formed by the complete fusion process was dominated by neutron evaporation channels. Combined ER cross sections for $2n$, $3n$, $4n$ and $5n$ contributes to more than 97% of CF for most of the beam energies. ER cross

sections were measured by recoil catcher technique followed by off-line gamma-ray spectrometry. Statistical model calculations were performed using PACE to quantitatively understand the ER cross sections, and estimate the contribution from the missing channels so as to obtain the experimental complete fusion cross sections. A comparison of the experimental data with ${}^6\text{Li} + {}^{144}\text{Sm}$ [3] showed that at above-barrier energies the CF cross sections are comparable but at sub-barrier energies they are largely enhanced for the present system. This implies that the effect of target deformation on sub-barrier fusion, i.e., enhancement is independent of whether the projectile is weakly- or strongly-bound. Coupled-channels calculations using CCFULL were performed to understand the measured CF data. At sub-barrier energies, the coupling of target deformation shows enhancements in CF cross sections and explain the data. However, at above-barrier energies there is a suppression of $28 \pm 4\%$ in the CF data compared to the CC calculations. The low energy threshold of the projectile seems to allow it to break up prior to fusion, leading to loss of flux from the entrance channel. It can therefore be concluded that the complete fusion cross section at energies above the barrier is suppressed due to projectile breakup. Thus the effects of both the target deformation as well as the projectile breakup are present, and their influence on each other seems to be negligible.

CF cross sections for the present system at above-barrier energies are found to be smaller by a factor $\sim 28\text{--}32\%$ than those calculated by Wong's formula using proximity potential, which is consistent with the above conclusion on fusion suppression. Comparison with the other systems involving strongly bound stable projectiles such as ${}^{12}\text{C} + {}^{141}\text{Pr}$ and ${}^{20}\text{Ne} + {}^{133}\text{Cs}$ forming similar compound nucleus also shows that CF cross sections for the present system at above-barrier energies are systematically lower compared to those with strongly bound projectiles, which further supports the above mentioned suppression. Since the CF cross sections at sub-barrier energies are slightly higher than those predicted by CC calculations, it may be assumed that the net effect of breakup (i.e., suppression due to loss of flux plus enhancement due to breakup coupling) is a small enhancement in fusion at this region.

CDCC calculations with projectile breakup channels reveal that the dynamic polarization potential generated due to breakup coupling is repulsive which leads to reduction in absorption cross section. Fusion cross sections obtained by both the cumulative absorption and BPM methods are found to be smaller compared to the ones with no breakup coupling, supporting the above conclusions on the effect of projectile breakup.

Present experimental data provide important input to the future realistic models of fusion with weakly bound projectiles to predict both qualitative and quantitative effects of projectile breakup at energies below as well as above Coulomb barrier energies, and how these effects get modified in the presence of large target deformation specially at sub-barrier energies where the deformation plays a significant role.

Acknowledgements

The authors would like to thank the pelletron crew for the smooth operation of the accelerator during the experiments. One of the authors P.K. Rath acknowledges the financial support of BRNS (No. 2007/37/7), India in carrying out these investigations.

References

- [1] L.F. Canto, P.R.S. Gomes, R. Donangelo, M.S. Hussein, Phys. Rep. 424 (2006) 1.
- [2] N. Keeley, R. Raabe, N. Alamanos, J.L. Sida, Prog. Part. Nucl. Phys. 59 (2007) 579.

- [3] P.K. Rath, S. Santra, N.L. Singh, R. Tripathi, V.V. Parkar, B.K. Nayak, K. Mahata, R. Palit, S. Kumar, S. Mukherjee, et al., *Phys. Rev. C* 79 (2009) R051601.
- [4] C.S. Palshetkar, S. Santra, A. Chatterjee, K. Ramachandran, S. Thakur, S.K. Pandit, K. Mahata, A. Shrivastava, V.V. Parkar, V. Nanal, *Phys. Rev. C* 82 (2010) 044608.
- [5] V.V. Parkar, R. Palit, S.K. Sharma, B.S. Naidu, S. Santra, P.K. Joshi, P.K. Rath, K. Mahata, K. Ramachandran, T. Trivedi, et al., *Phys. Rev. C* 82 (2010) 054601.
- [6] K. Rusek, N. Alamanos, N. Keeley, V. Lapoux, A. Pakou, *Phys. Rev. C* 70 (2004) 014603.
- [7] K. Rusek, *Eur. Phys. J. A* 41 (2009) 399.
- [8] R. Beringer, *Phys. Rev. Lett.* 18 (1967) 1006.
- [9] C.Y. Wong, *Phys. Lett. B* 42 (1972) 186.
- [10] C.Y. Wong, *Phys. Rev. Lett.* 31 (1973) 766.
- [11] M. Hussein, L.F. Cantoa, R. Donanagelo, *Phys. Rev.* 21 (1980) 772.
- [12] R.G. Stokstad, Y. Eisen, S. Kaplanis, D. Pelte, U. Smilansky, I. Tserruya, *Phys. Rev. C* 21 (1980) 2427.
- [13] R.G. Stokstad, Y. Eisen, S. Kaplanis, D. Pelte, U. Smilansky, I. Tserruya, *Phys. Rev. Lett.* 41 (1978) 465.
- [14] R.G. Stokstad, W. Reisdorf, K.D. Hildenbrand, J.V. Kratz, G. Wirth, R. Lucas, J. Poitou, *Z. Phys. A* 295 (1980) 269.
- [15] J.R. Leigh, M. Dasgupta, D.J. Hinde, J.C. Mein, C.R. Morton, R.C. Lemmon, J.P. Lestone, J.O. Newton, H. Timmers, J.X. Wei, et al., *Phys. Rev. C* 52 (1995) 3151.
- [16] P.R.S. Gomes, I.C. Charret, R. Wanis, G.M. Sigaud, V.R. Vanin, R.L. Neto, D. Abriola, O.A. Capurro, D.E. DiGregorio, M. di Tada, et al., *Phys. Rev. C* 49 (1994) 245.
- [17] W. Reisdorf, F.P. Hessberger, K.D. Hildenbrand, S. Hofmann, G. Mnzenberg, K.H. Schmidt, J.H.R. Schneider, W.F.W. Schneider, K. Smmerer, G. Wirth, et al., *Nucl. Phys. A* 438 (1985) 212.
- [18] M. Trotta, A. Stefanini, L. Corradi, E. Fioretto, A. Gadea, S. Szilner, S. Beghini, G. Montagnoli, F. Scarlassara, A. Chizhov, et al., *Nucl. Phys. A* 734 (2004) 245.
- [19] P.N. Rowley, G.R. Satchler, *Phys. Lett. B* 254 (1991) 25.
- [20] M. Dasgupta, D. Hinde, N. Rowley, A. Stefanini, *Ann. Rev. Nucl. Part. Sc.* 48 (1998) 401.
- [21] H. Holm, W. Scheid, W. Greiner, *Phys. Lett. B* 29 (1969) 473.
- [22] P.W. Riesenfeldt, T.D. Thomas, *Phys. Rev. C* 02 (1970) 711.
- [23] B.B. Back, R.R. Betts, W. Henning, K.L. Wolf, A.C. Mignerey, J.M. Lebowitz, *Phys. Rev. Lett.* 45 (1980) 1230.
- [24] S. Santra, P. Singh, S. Kailas, A. Chatterjee, A. Shrivastava, K. Mahata, *Phys. Rev. C* 64 (2001) 024602.
- [25] S. Santra, P. Singh, S. Kailas, A. Chatterjee, A. Navin, A. Shrivastava, A.M. Samant, K. Mahata, *Phys. Rev. C* 60 (1999) 034611.
- [26] N. Keeley, K. Rusek, *Phys. Rev. C* 56 (1997) 3421.
- [27] S. Santra, S. Kailas, K. Ramachandran, V.V. Parkar, V. Jha, B.J. Roy, P. Shukla, *Phys. Rev. C* 83 (2011) 034616.
- [28] F. Plasil, R.L. Ferguson, R.L. Hahn, F.E. Obenshain, F. Pleasonton, G.R. Young, *Phys. Rev. Lett.* 45 (1980) 333.
- [29] R. Kossakowski, J. Jastrzebski, P. Rymuza, W. Skulski, A. Gizon, S. Andre, J. Genevey, J. Gizon, V. Barci, *Phys. Rev. C* 32 (1985) 1612.
- [30] J.K. Tuli, Nuclear Wallet Card, National Nuclear Data Center, <http://www.nndc.bnl.gov/nudat2/>, 2000.
- [31] A. Gavron, *Phys. Rev. C* 21 (1980) 230.
- [32] C.M. Perey, F.G. Perey, *Atm. Data. Nucl. Data Tables* 17 (1976) 1.
- [33] J.R. Huizenga, G. Igo, *Nucl. Phys.* 29 (1962) 462.
- [34] D. Hill, J. Wheeler, *Phys. Rev. C* 89 (1953) 1102.
- [35] P.R.S. Gomes, J. Lubian, I. Padron, R.M. Anjos, *Phys. Rev. C* 71 (2005) 017601.
- [36] K. Hagino, N. Rowley, A.T. Kruppa, *Comput. Phys. Commun.* 123 (1999) 143.
- [37] R.A. Broglia, A. Winther, Heavy Ion Reaction Lecture Notes I, Benjamin Cummings, Redwood City, CA, 1981, p. 114.
- [38] U. Gotz, H.C. Pauli, K. Alder, K. Junker, *Nucl. Phys. A* 192 (1997) 1.
- [39] C. Beck, F.A. Souza, N. Rowley, S.J. Sanders, N. Aissaoui, E.E. Alonso, P. Bednarczyk, N. Carline, S. Courtin, A. DiazTorres, et al., *Phys. Rev. C* 67 (2003) 054602.
- [40] J. Blocki, J. Randrup, W.J. Swiatecki, C.F. Tsang, *Ann. Phys. (NY)* 105 (1977) 427.
- [41] W. Reisdorf, *J. Phys. G: Nucl. Part. Phys.* 20 (1994) 1297.
- [42] I. Dutt, R.K. Puri, *Phys. Rev. C* 81 (2010) 064608.
- [43] P. Moller, J.R. Nix, *Nucl. Phys. A* 361 (1981) 117.
- [44] P. Moller, J.R. Nix, W.D. Myers, W.J. Swiatecki, *At. Data Nucl. Data Tables* 59 (1995) 185.
- [45] W.D. Myers, W.J. Swiatecki, *Phys. Rev. C* 62 (2000) 044610.
- [46] I.J. Thompson, *Comput. Phys. Rep.* 7 (1988) 167.
- [47] P. Christensen, A. Berinde, I. Neamu, N. Scintei, *Nucl. Phys. A* 129 (1969) 337.

- [48] E. Obiajunwa, L.H. Rosier, J.V. de Wiele, Nucl. Phys. A 500 (1989) 341.
- [49] H. Nishioka, J.A. Tostevin, R.C. Johnson, K.I. Kubo, Nucl. Phys. A 415 (1984) 230.
- [50] A. Diaz-Torres, I.J. Thompson, C. Beck, Phys. Rev. C 68 (2003) 044607.